

Interplay of anomalous strain relaxation and minimization of polarization changes at nitride semiconductor heterointerfaces

Y. Wang,^{1,2} M. Schnedler^{1,*}, Q. Lan,^{1,3} F. Zheng,³ L. Freter^{1,2}, Y. Lu,³ U. Breuer⁴, H. Eisele,⁵ J.-F. Carlin,⁶ R. Butté⁶, N. Grandjean,⁶ R. E. Dunin-Borkowski^{1,3} and Ph. Ebert^{1,†}

¹*Peter Grünberg Institut, Forschungszentrum Jülich GmbH, 52425 Jülich, Germany*

²*Lehrstuhl für Experimentalphysik IV E, RWTH Aachen University, 52056 Aachen, Germany*

³*Ernst Ruska Centrum, Forschungszentrum Jülich GmbH, 52425 Jülich, Germany*

⁴*Zentralinstitut für Engineering, Elektronik und Analytik (ZEA-3), Forschungszentrum Jülich GmbH, 52425 Jülich, Germany*

⁵*Institut für Festkörperphysik, Technische Universität Berlin, Hardenbergstrasse 36, 10623 Berlin, Germany*

⁶*Institute of Physics, Ecole Polytechnique Fédérale de Lausanne, 1015 Lausanne, Switzerland*



(Received 18 August 2020; revised 4 November 2020; accepted 1 December 2020; published 21 December 2020)

We present a methodology to quantify polarization and electron affinity changes at interfaces by combining scanning tunneling spectroscopy, off-axis electron holography in transmission electron microscopy (TEM), and self-consistent calculations of the electrostatic potential and electron phase change. We use a precisely known grown-in doping structure to calibrate the surface potential of the TEM lamella and thereby achieve a quantitative analysis of electron phase changes measured by off-axis electron holography. Using this calibration, we deduce quantitatively polarization and electron affinity changes for $\text{Al}_{0.06}\text{Ga}_{0.94}\text{N}/\text{GaN}$ and $\text{In}_{0.05}\text{Ga}_{0.95}\text{N}/\text{Al}_{0.06}\text{Ga}_{0.94}\text{N}$ interfaces. The latter interface reveals, as expected, biaxial relaxation as well as polarization and electron affinity changes. However, at the $\text{Al}_{0.06}\text{Ga}_{0.94}\text{N}/\text{GaN}$ interface anomalous lattice relaxations and vanishing polarization and electron affinity changes occur, whose underlying physical origin is anticipated to be total energy minimization by the minimization of Coulomb interactions between the polarization-induced interface charges.

DOI: [10.1103/PhysRevB.102.245304](https://doi.org/10.1103/PhysRevB.102.245304)

I. INTRODUCTION

Group III nitride semiconductors became the material system of choice for solid-state lighting and high-power semiconductor devices. Functioning of such devices is highly dependent on the presence and characteristics of doping and/or heterointerfaces. However, such interfaces may introduce new localized features: Besides lattice mismatch-induced strain, interdiffusion, and segregation, interfaces typically lead to a variety of localized electronic properties, such as atomically localized electronic states, band offsets, and polarization changes. These localized electronic features and, particularly, polarization changes, giving rise to two-dimensional sheets of bound charges [1,2], are partly desired (e.g., in high electron mobility transistors), but partly, they have the potential to affect, e.g., quantum wells and hence device performance adversely [3].

Thus far, polarization fields in group III nitride semiconductors grown along the c direction have been considered to be the most critical problem for spatial carrier separation in quantum wells. In order to avoid such polarization fields, growth on nonpolar or semipolar planes flourished [4]. However, polarization fields in the c direction and their detrimental effects on quantum wells can be avoided, too, by so-called polarization matching, i.e., by adjusting ternary or quaternary

compositions to tune the polarization of the barrier materials relative to that of the quantum well [3,5]. This strategy, allowing the removal of polarization changes at interfaces, implicitly assumes that composition in conjunction with linear elastic biaxial strain at the interfaces fully determine the polarization. However, this approach ignores a possible interplay between the polarization, charge sheets, and the lattice relaxation at interfaces, potentially creating unexpected interface polarization and relaxation structures.

Here we quantitatively probe polarization and electron affinity changes at group III nitride heterointerfaces by combining off-axis electron holography, scanning tunneling spectroscopy, and self-consistent simulations. Although some interfaces exhibit the expected polarization change and biaxial lattice strain, we unravel, against expectations, for another interface anomalous lattice relaxations combined with a disappearance of polarization change. We argue that the driving force for the anomalous relaxation is the minimization of the total energy by reduction of the Coulomb interaction energy between bound charges arising from polarization changes at the heterointerfaces. Such effects have the potential to critically change the efficiencies of devices based on interfaces with anomalous relaxation and polarization changes.

II. METHODS

For this work we needed to probe quantitatively the polarization change and lattice relaxation at interfaces. It is,

*m.schnedler@fz-juelich.de

†p.ebert@fz-juelich.de

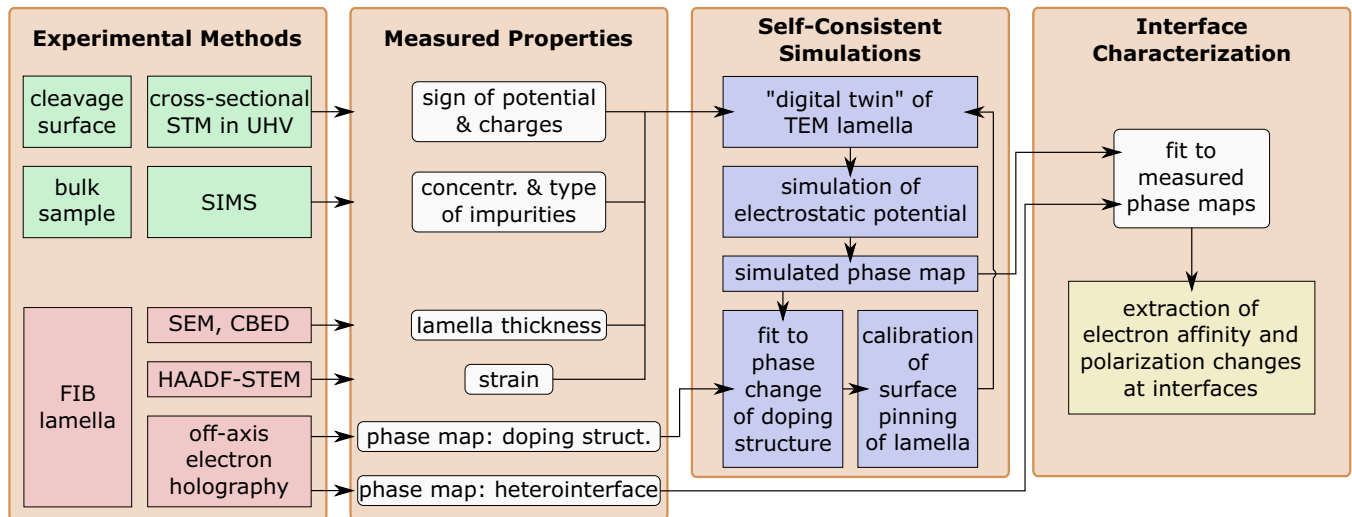


FIG. 1. Schematic overview of the experimental and theoretical methodology.

however, a rather difficult task to probe electronic properties directly at interfaces with atomic resolution. Thus far, the only microscopic access to electronic states and structures at interfaces has been achieved by cross-sectional scanning tunneling microscopy (STM) and spectroscopy (STS) [6–8] or by off-axis electron holography in transmission electron microscopy (TEM) [9–15]. Both methods can provide access to the local electronic properties, although each one is insufficient for a comprehensive physical understanding of nitride heterointerfaces. On the one hand, the interpretation of tunneling spectra is surprisingly complex and problematic in the case of nitride semiconductor cleavage surfaces since valence band states are invisible [16] and the empty surface state provides a Fermi level pinning in the band gap [17]. Hence, quantifying potential fluctuations in nitride semiconductors is extraordinarily challenging and has not been achieved thus far, in contrast to other materials where the STS/STM technique was exceptionally successful in mapping the electrostatic potential [6,18,19]. On the other hand, off-axis electron holography in a TEM provides direct access to the local electrostatic potential integrated along the electron beam direction. However, the measured potential is highly sensitive to the sample preparation. In particular, the presence of a so-called dead layer near the surfaces can severely alter the measured potential and hence the phase of the transmitted electrons [20,21]. As a result, none of these methods taken alone provides the complete picture of electronic properties at ternary III-N interfaces.

Therefore, we characterize the electronic properties of different III-N semiconductor interfaces by combining STM/STS, off-axis electron holography in TEM, secondary-ion mass spectrometry (SIMS), and self-consistent simulations of the electrostatic potential and the electron phase (see schematic overview in Fig. 1). The central weakness of off-axis electron holography applied to semiconductors is the lack of knowledge of the potential near the surface regions of the electron transparent lamellae. Hence, the quantification of the surface potential is the critical task to achieve a quantitative interpretation of the electron phase measured by off-axis electron holography.

In order to tackle this problem, we used a δ -type doping structure for calibration of the effect of the Fermi level pinning at the surfaces of the thin TEM lamella on the phase change of the transmitted electrons in electron holography: This requires full *a priori* knowledge of all properties affecting the electrostatic potential, such that the only remaining parameter is the pinning level of the Fermi energy at the lamella's surfaces. This full *a priori* knowledge can be achieved only for a doping structure; that is, in our case we use a δ -type doping structure.

Here come into action two additional experimental methods, as illustrated in the schematic overview in Fig. 1: STS is used to determine the sign of the potential change and the sign of the fixed (localized) charge at the δ -type doping layer. This allows us to conclude that the origin of the potential change is due to *n*-type dopants (not defects) and to quantify the microscopic width of the doping structure. Furthermore, this provides a calibration of the sign of the phase change in electron holography. Finally, the type and concentration of doping impurity are quantified by SIMS to obtain the missing quantitative values needed for the self-consistent calculation of the electrostatic potential and the resulting phase change as a function of the surface pinning level. Fitting the simulation to the measured phase profile of the δ -type doping structure provides a quantitative determination of the surface pinning, which is used as a basis for quantifying all further interfaces.

The investigated heterostructure, grown by metal organic vapor phase epitaxy on a *c*-plane freestanding hydride vapor phase epitaxy-grown GaN substrate (carrier concentration $\sim 10^{18} \text{ cm}^{-3}$), consists of a 700-nm GaN buffer doped with $3 \times 10^{18} \text{ cm}^{-3}$ Si, 750-nm $\text{Al}_{0.06}\text{Ga}_{0.94}\text{N}$ doped with $5 \times 10^{18} \text{ cm}^{-3}$ Si, followed by 100-nm $\text{In}_{0.05}\text{Ga}_{0.95}\text{N}$ ($3 \times 10^{18} \text{ cm}^{-3}$ Si). For cross-sectional STM/STS measurements samples cut from the heterostructure were cleaved in ultrahigh vacuum (1×10^{-8} Pa) along (10 $\bar{1}$ 0) planes and directly investigated by STM. For TEM measurements electron transparent lamellae (with [10 $\bar{1}$ 0] being the normal vector) were prepared by focused ion beam (FIB) milling in a FEI Helios Nanolab 400 s dual-beam system using Ga ions. The thickness measurements are discussed in detail in Sec. III A. The lamellae were then investigated by off-axis

electron holography in an image-aberration-corrected FEI Titan G2 60-300 HOLO microscope [22] at an acceleration voltage of 300 kV. The lattice parameters of the sample were measured by high-angle annular dark-field scanning transmission electron microscopy (HAADF-STEM) imaging on a FEI Titan G2 80-200 ChemiSTEM microscope equipped with a high-brightness field emission gun (XFEG) and a probe aberration corrector [23]. The nominal lattice constants of the GaN substrate were used to calibrate measured local lattice parameters. Time-of-flight secondary-ion mass spectrometry (TOF.SIMS 5, NCS IONTOF GmbH) was used to determine the Si doping concentration throughout the heterostructure. To measure the heterostructures' depth profile a Cs beam (1 keV, 90 nA) was used to remove material within an area of $300 \times 300 \mu\text{m}^2$, followed by a pulsed 30-keV Bi^+ ion beam for sampling the chemical composition of an area of $50 \times 50 \mu\text{m}^2$ in the center of the larger area.

For self-consistent simulation of the phase changes at interfaces measured by off-axis electron holography, we used the finite-difference-based Poisson solver described in Refs. [24,25]: In order to incorporate polarization \vec{P} changes at interfaces, the Poisson equation (Eq. (3) in Ref. [24]) is extended to $\Delta V_{\text{EP}}(x, y, z) = -\frac{e}{\epsilon_0 \epsilon_r} \times [\rho(x, y, z) - \vec{\nabla} \cdot \vec{P}]$, where $V_{\text{EP}}(x, y, z)$ is the three-dimensional electrostatic potential, e is the elementary charge, ϵ_0 and ϵ_r are the vacuum and material's relative permittivity, respectively, and $\rho(x, y, z)$ denotes the charge density (consisting of free charges and fixed ionized donors). Note that here polarization always refers to the sum of piezoelectric and spontaneous polarization. In addition, the boundary condition was extended by including the polarization change times the normal vector of the interface, leading to a bound sheet charge σ_b at the interface (in analogy to Eq. (17) in Ref. [24]). The thus obtained electrostatic potential V_{EP} is added to the mean inner potential V_{MIP} calculated by density functional theory [26]. The phase ϕ is given as the integral (or projection) of the potential along the electron beam (z direction) from the electron source to the detector,

$$\phi = \int_{-\infty}^{\infty} C_E \times (V_{\text{EP}} + V_{\text{MIP}}) dz, \quad (1)$$

where $C_E = e/(\hbar \times v_e)$ is a constant that depends on the relativistic electron velocity v_e [27]. \hbar denotes the reduced Planck's constant. For practical purposes we set the integration range to the width of the equidistant finite-difference grid used in the Poisson solver. Furthermore we assume that the electron beam does not modify the charge distribution within the semiconductor. The sign conventions in this paper are as follows: A negative charge increases locally the electrostatic potential V_{EP} , while it decreases the phase ϕ .

III. RESULTS

Figure 2 shows an overview STM image and, in the inset, a phase image, reconstructed from electron holograms [15], of the $\text{Al}_{0.06}\text{Ga}_{0.94}\text{N}/\text{GaN}$ buffer/GaN layers of the heterostructure. The additional 100-nm $\text{In}_{0.05}\text{Ga}_{0.95}\text{N}$ layer on top in the $[0001]$ direction is outside of the field of view. Thus, one can distinguish here two interfaces from changes in contrast: In the STM images, the GaN buffer/substrate interface

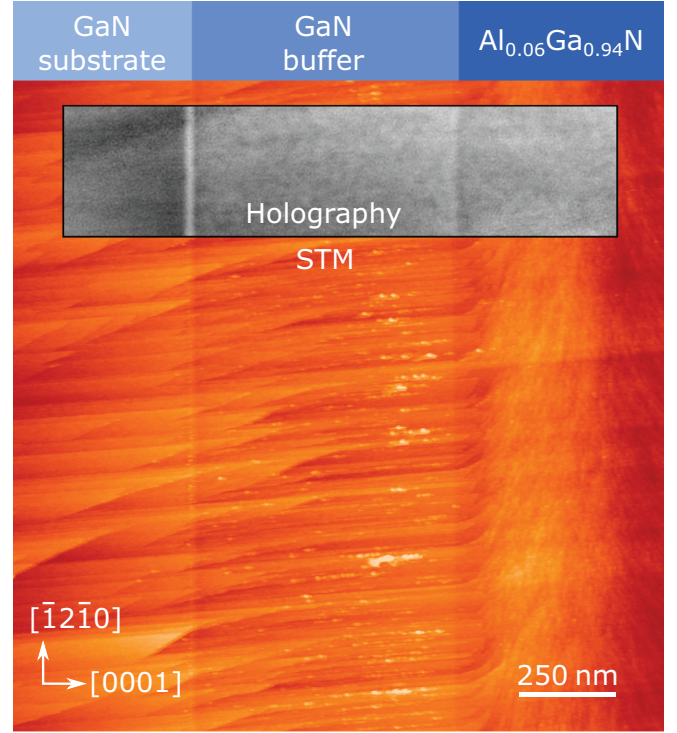


FIG. 2. Cross-sectional constant-current STM overview image of the $(10\bar{1}0)$ cleavage surface through the $\text{Al}_{0.06}\text{Ga}_{0.94}\text{N}/\text{GaN}$ buffer/GaN substrate heterostructure measured at -2.5 V and 80 pA. The inset shows an image of the phase of the transmitted electrons acquired by off-axis electron holography in a transmission electron microscope (m direction view, tilt angles of 13° and 1° in the a and c directions, respectively). On the left-hand side, part of the GaN substrate is visible, as indicated at the top edge. One can distinguish two interfaces from changes in contrast in both images. The GaN buffer to substrate interface exhibits a bright contrast, whereas the $\text{Al}_{0.06}\text{Ga}_{0.94}\text{N}/\text{GaN}$ interface reveals a steplike contrast change. In addition to the interface contrast, one can observe cleavage steps in the STM image. The steps are oriented preferentially in the $[0001]$ direction in the GaN substrate and buffer, whereas a pronounced turning is observed in the $\text{Al}_{0.06}\text{Ga}_{0.94}\text{N}$ layer.

appears bright, whereas the $\text{Al}_{0.06}\text{Ga}_{0.94}\text{N}/\text{GaN}$ interface is characterized by a change in height. Similarly, in the phase image the GaN buffer to substrate interface exhibits a bright contrast, i.e., a positive local change in the phase, whereas the $\text{Al}_{0.06}\text{Ga}_{0.94}\text{N}/\text{GaN}$ interface reveals a steplike change in the phase. In the following we first address the GaN substrate to buffer interface and then analyze the $\text{Al}_{0.06}\text{Ga}_{0.94}\text{N}/\text{GaN}$ interface and the further $\text{In}_{0.05}\text{Ga}_{0.95}\text{N}/\text{Al}_{0.06}\text{Ga}_{0.94}\text{N}$ interface using the methods and understanding developed for the former interface.

A. GaN buffer/substrate interface

The inset in Fig. 3 illustrates the Si concentration profile at the GaN buffer/substrate interface measured by SIMS. Directly at the interface a δ -type doping peak is present, followed by a dip on the buffer side before a constant level is reached. In addition, Fig. 3 displays as gray symbols the phase change across the GaN buffer-substrate interface, reconstructed from

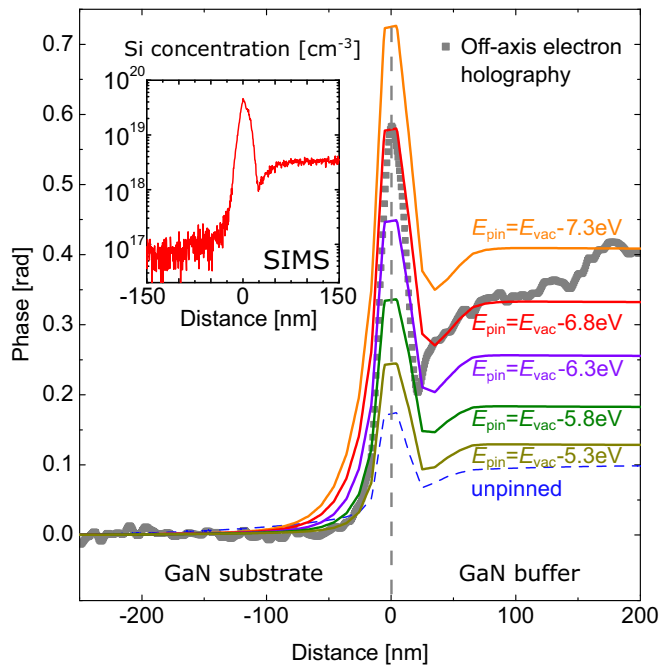


FIG. 3. Average profile of the phase change (gray symbols) across the GaN buffer/GaN substrate interface measured by off-axis electron holography. The lines represent self-consistent calculations of the phase change for different surface pinning conditions. The best agreement between simulated and measured phase change, taking the Si doping concentration measured by SIMS (inset) into account, is achieved for a surface pinning at $E_{\text{vac}} - (6.8 \pm 0.2)$ eV, i.e., $E_V + (0.69 \pm 0.2)$ eV. The pinning level is consistent with the (+/3+) charge transition level of N vacancies calculated to be at $E_V + 0.5$ eV [28–31]. This suggests that N vacancies are introduced in the near-surface region of the TEM lamella during FIB cutting (see text).

electron holograms. Furthermore, Figs. 4(a)–4(c) display selected tunneling spectra across the GaN buffer-substrate interface, a current-imaging tunneling spectroscopy (CITS) map at +2.5 V, and line profiles of the current at +2.28 V and the voltage reached at +20 pA, respectively.

First of all, one can observe a rather obvious similarity between the current line profile measured by STM [blue line in Fig. 4(c)], the Si concentration (measured by SIMS, inset in Fig. 3), and the phase change profiles in terms of the width of the peak at the interface and the decrease directly beside the main peak on the GaN buffer side (gray symbols in Fig. 3).

Second, the CITS map and its line profile [Figs. 4(b) and 4(c)] exhibit a bright contrast at the interface. In addition, the tunneling spectra reveal a shift of the positive voltage branch toward smaller voltages at the interface. Since at positive voltages electrons tunnel into the empty conduction band states of GaN [16], the shift toward smaller voltages indicates a local downward band bending with a spatial full width at half maximum (FWHM) of ~ 20 nm arising from positively charged impurities at or near the interface. In n -type semiconductors, this downward band bending is compatible only with donor impurities, such as Si. The charge sign and the width of the interface layer in STM are also in agreement with the large Si concentration peak up to $5 \times 10^{19} \text{ cm}^{-3}$ revealed by SIMS.

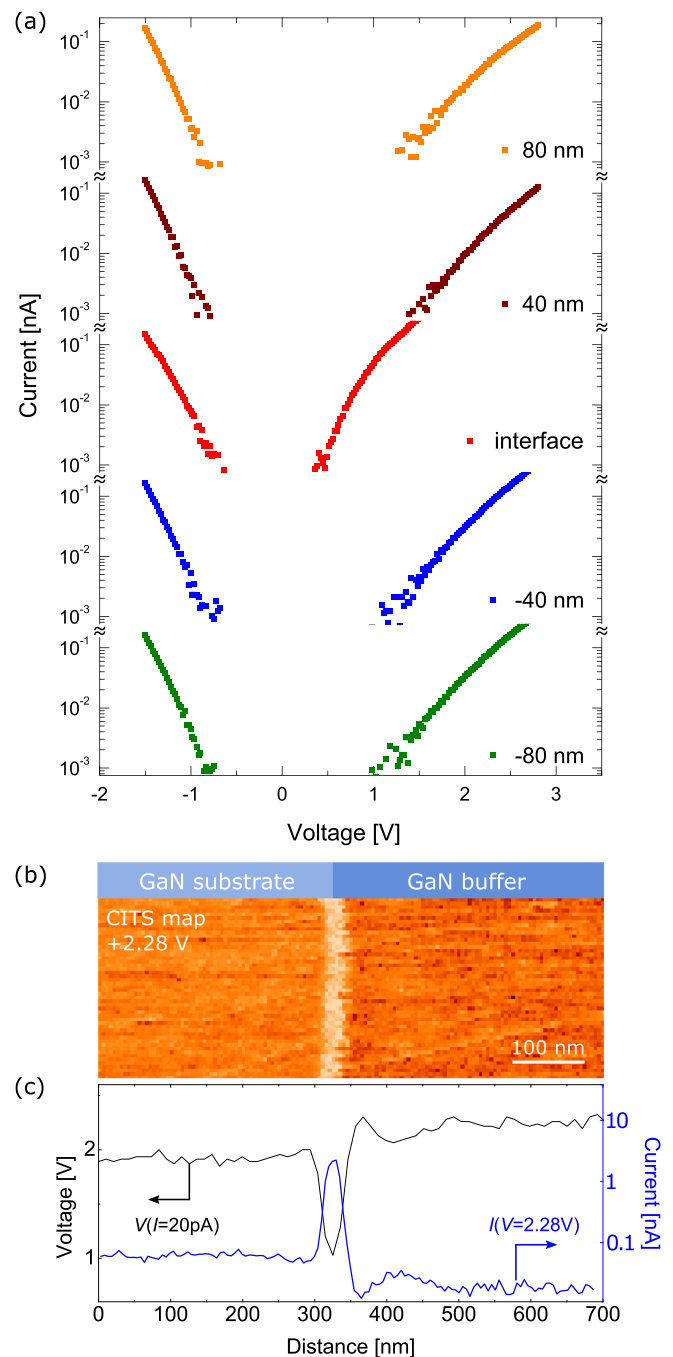


FIG. 4. (a) Current-voltage tunnel spectra measured across the GaN buffer/GaN substrate interface. The tunnel current onset on the positive branch is shifted to smaller positive voltages near the interface, indicating a downward band bending. (b) Current-imaging tunneling spectroscopy (CITS) map, evaluated at +2.5 V. (c) Line profiles of the current (blue line) at +2.28 V obtained from the CITS map and of the voltage at which a current of +20 pA is reached (black line). Both profiles and the CITS map reveal a 20-nm-wide region with downward band bending.

In addition, the positive phase change peak, also having a FWHM of ~ 20 nm, indicates a downward electrostatic potential change at the interface too, corroborating the charge sign probed by STM. This suggests that most of the phase contrast

is, indeed, related to the Si doping peak present at the GaN buffer-substrate interface.

At this stage, we exclude possible further effects, notably materials changes, beam-induced electron-hole pairs, thickness changes, charging, drifts, and diffraction effects, which may also contribute to the phase change in the transmitted electrons.

(i) The concentration of beam-induced electron-hole pairs is roughly one order of magnitude or more lower than the doping concentration [32]. Hence, the effect of beam-induced electron-hole pairs on the electrostatic potential can be neglected here.

(ii) Cutting of the lamellae by FIB may introduce changes in the sample thickness. However, the beam direction of the FIB was perpendicular to the interfaces, and thus, weak thickness modulations occur only along the interfaces in a direction. Hence, the phase profiles across the interfaces are not affected by sudden changes in the thickness near the interface.

(iii) For beam-induced charging, the phase exhibits an approximately linear background. This is assigned to possible charging of the Au layer present on the terminal (0001) growth surface. The short-range effects observed near the interfaces are superimposed onto the linear background, which can be rather easily subtracted in the vicinity of the interfaces.

We conclude that the phase change at the interface has primarily an electrostatic potential origin. In order to verify this assumption, we made simulations of the phase of transmitted electrons based on the electrostatic potential distribution assuming different physical conditions. For this we calculated the macroscopic electrostatic potential (for details see Sec. II) using the Si doping concentrations measured by SIMS (inset in Fig. 3) for different surface potentials fixed by Fermi level pinning at the surfaces of the TEM lamella.

In order to specify which surface at the TEM lamella is relevant, we turn to the thickness of the TEM lamella (which is a central parameter for simulation). The total thickness was determined by scanning electron microscopy (SEM) to 296.4 ± 1.3 nm, whereas the crystalline thickness was extracted by convergent beam electron diffraction (CBED) to 277.9 ± 2 nm (see Fig. 1). This indicates that the samples have an amorphous top surface layer approximately 9 nm thick. In the following we assume that the amorphous layer is everywhere identical (and well intermixed) and thus creates only a constant offset of the phase throughout the whole sample and no localized changes in the electron phase at the interfaces. The changes in the electron phase at these interfaces are thus solely governed by the electrostatic potential and mean inner potential (MIP) in the crystalline part of the TEM lamella. The electrostatic potential is affected by Fermi level pinning in the transition region between the crystalline and amorphous parts of the TEM lamella. This is hence the effective electronic surface of the TEM lamella in electron holography, and thus, we call it, for simplification in the following, the “surface” of the TEM lamella. On this basis we calculate the spatial change in the phase of the transmitted electrons using Eq. (1) for the crystalline thickness under consideration of the tilt angles.

Figure 3 shows the calculated phase profiles for different surface pinning levels, in comparison to the experimentally measured phase across the GaN buffer-substrate interface (gray symbols). First, we address the case of an ideal sur-

face without any surface state in the fundamental band gap (blue dashed line). In this case only the small differences in band edge position for different doping levels contribute to the electrostatic potential and hence create a small phase change in transmitted electrons. The peak height is much too small to account for the measured phase change. Hence, the surfaces of the TEM lamella cannot be free of surface states in the band gap. Therefore, we assumed a pinning at the surfaces of the lamella. The peak height is now found to increase with the decreasing pinning level. The optimum pinning level is (6.8 ± 0.2) eV below the vacuum energy E_{vac} , i.e., $E_V + (0.69 \pm 0.2)$ eV, with E_V being the valence band edge. Hence, the large peak intensity indicates that pinning at the surfaces of the TEM lamella is a critical factor. In fact, recently, a phase change of 0.6 rad between 5×10^{19} and 5×10^{18} cm $^{-3}$ doped GaN (350-nm thick lamella) was measured [33]. This value is also much higher than expected without surface pinning, corroborating our conclusion.

At this stage we turn to the origin of pinning near the surfaces of the TEM lamella. We recall that after FIB preparation, the lamella is taken out of the FIB vacuum system into ambient air. This leads to an adsorbate (oxygen) coverage at the lamellae’s amorphous surfaces. The adsorbates, oxidation, and amorphous layer can be expected to induce midgap pinning states. However, midgap pinning would not be compatible with the observed phase peak height. In a second step one has to consider the types of defects in the near-surface crystalline regions of the lamella (i.e., below the oxidized and partially amorphous surface) created by the Ga ion beam used for cutting the lamella. The ion beam can be expected to create N and Ga vacancies and interstitial atoms. Since N is much lighter than Ga, most ion-induced defects will be related to the displacement of N atoms but not of Ga atoms. Furthermore, the diffusion energies of the defects differ considerably, with the highest diffusion barrier of ~ 4 eV for N vacancies [29,30]. One can thus anticipate N vacancies will be the dominant defect in the crystalline near-surface region, while all interstitial atoms and Ga vacancies will be incorporated into the amorphous cover layer. Thus, we consider the charge transition levels of N vacancies: All charge transition levels except one are either very close to or above the conduction band edge or in the valence band and thus electrically inactive in our case. The only electrically active charge transition level is the (+/3+) level, which is found in the band gap at $E_V + 0.5$ eV [28–31]. This level agrees well with the pinning level of the crystalline near-surface region of the TEM lamella, derived from the measured phase change. Note that, unfortunately, the methodology used here is not capable of resolving single point defects, and hence, the conclusion about the origin of the Fermi level pinning cannot be corroborated microscopically.

B. $\text{Al}_{0.06}\text{Ga}_{0.94}\text{N}/\text{GaN}$ buffer interface

At this stage we address the $\text{Al}_{0.06}\text{Ga}_{0.94}\text{N}/\text{GaN}$ buffer interface, which gives rise to a steplike change in the phase map (gray symbols in Fig. 5). The steplike phase change can be understood as follows: In a semiconductor with sufficiently large doping concentrations, i.e., with efficient screening of the electrostatic potential, a steplike phase change is indicative of an effect that is not only present locally at the interface but

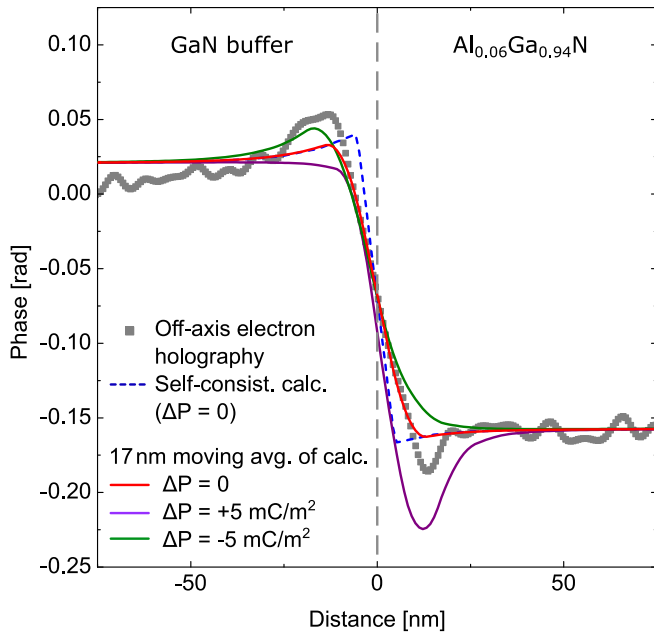


FIG. 5. Average phase change profile (gray symbols) across the $\text{Al}_{0.06}\text{Ga}_{0.94}\text{N}/\text{GaN}$ buffer interface measured by off-axis electron holography. The lines represent different self-consistent calculations of the phase change. The step-function shape of the phase change is attributed to (i) a mean inner potential change ΔV_{MIP} between the two materials and (ii) a change in the electron affinity $\Delta\chi$. The best agreement is achieved for $\Delta V_{\text{MIP}} = 105$ mV and $\Delta\chi = +43 \pm 50$ meV (see red solid line). Note that due to the tilt of the sample to avoid a diffraction contrast a broadening occurs, which was taken into account by applying a 17-nm moving average to the simulated phase signal (see red solid line vs. blue dashed line). In addition, two further simulations are shown (purple and green solid lines), which include a polarization change at the interface of ± 5 mC/m². With the polarization change the experimental shape near the step edge of the phase is not well reproduced. This indicates that no significant polarization change occurs. The surface pinning level is the same as for the GaN substrate/buffer interface.

extends over all adjacent layers. Thus, local interface states or sheets of charges, e.g., due to polarization, can be ruled out. Unlike the above GaN buffer/GaN substrate interface, the carrier concentrations on both sides of the $\text{Al}_{0.06}\text{Ga}_{0.94}\text{N}/\text{GaN}$ interface are similar (5×10^{18} and 3×10^{18} Si atoms/cm³, respectively), and thus, the step-function-like behavior cannot be solely explained by a change in the doping concentration. Hence, the measured phase shift is attributed to (i) MIP change (the material's contrast) and (ii) a change in electron affinity between $\text{Al}_{0.06}\text{Ga}_{0.94}\text{N}$ and GaN.

First, we determined the MIP of the ternary compounds from the calculated values of the binary compounds [26] using Vegard's law. Furthermore, we took into account the fact that the strain compresses or expands the atomic lattice, resulting in a deviation of the MIP from its unstrained equilibrium value. The strained MIP is scaled to the atom density determined from the lattice constant measurements by high-resolution HAADF-STEM (see Sec. III D). This yields a MIP change at the interface of $\Delta V_{\text{MIP}} = 105 \pm 32$ mV. On this basis, the best agreement of self-consistent calculations

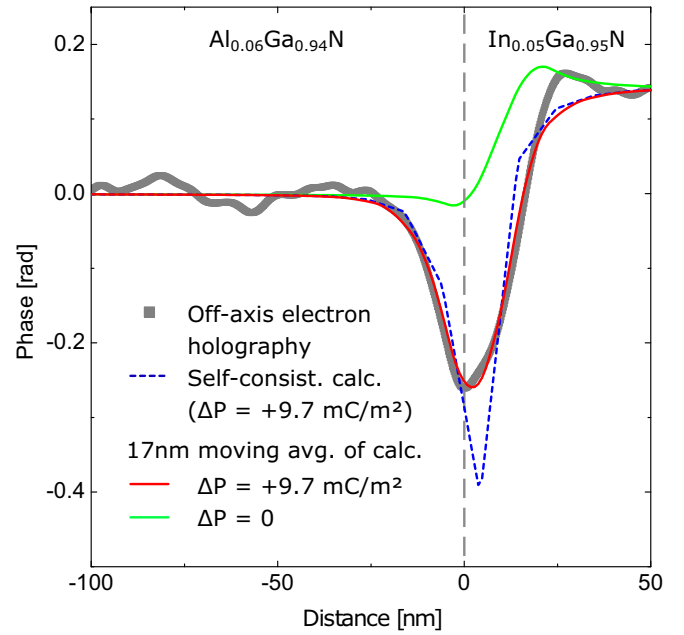


FIG. 6. Average phase change (gray symbols) measured across the $\text{In}_{0.05}\text{Ga}_{0.95}\text{N}/\text{Al}_{0.06}\text{Ga}_{0.94}\text{N}$ interface and self-consistent calculations (lines). The phase profile exhibits a pronounced depression in addition to a step-function-like behavior at the interface. The step-function-like behavior arises from changes in the mean inner potential ($\Delta V_{\text{MIP}} = 281$ mV) and the electron affinity ($\Delta\chi = +170 \pm 50$ meV; green solid line). The depression indicates the presence of a charge sheet due to a polarization change. The best agreement is obtained for a polarization change of $+9.7 \pm 2.0$ mC/m² (red solid line). The broadening due to the tilting of the zone axis was taken into account again using a 17-nm moving average. The surface pinning level is the same as for the other interfaces.

of the phase with the experimentally measured phase profile is obtained for an electron affinity change of $\Delta\chi = +43 \pm 50$ meV and no polarization change (red solid line in Fig. 5). In order to assess the sensitivity of the phase change on polarization, we performed self-consistent simulations including a polarization change of ± 5 mC/m² (see purple and green solid lines in Fig. 5). The computed phase profiles with polarization do not reproduce the shape near the step. Therefore, we obtain a polarization change of $\Delta P = 0 \pm 2$ mC/m². Note that the quantitative analysis of the phase change is possible only due to the prior calibration of the surface pinning achieved for the δ -doped structure at the GaN buffer-substrate interface. Without such an internal calibration the dead surface layer inhibits any meaningful quantitative interpretation.

C. $\text{In}_{0.05}\text{Ga}_{0.95}\text{N}/\text{Al}_{0.06}\text{Ga}_{0.94}\text{N}$ interface

The measured phase change profile across the $\text{In}_{0.05}\text{Ga}_{0.95}\text{N}/\text{Al}_{0.06}\text{Ga}_{0.94}\text{N}$ interface (gray symbols in Fig. 6) is analyzed in analogy to the interfaces discussed above. The phase exhibits a pronounced depression, in addition to a step-function-like behavior at the interface. The latter can be explained in analogy to the $\text{Al}_{0.06}\text{Ga}_{0.94}\text{N}/\text{GaN}$ interface by a change in the mean inner potential ($\Delta V_{\text{MIP}} = 281 \pm 40$ mV) and in the electron affinity ($\Delta\chi = +170 \pm 50$ meV).

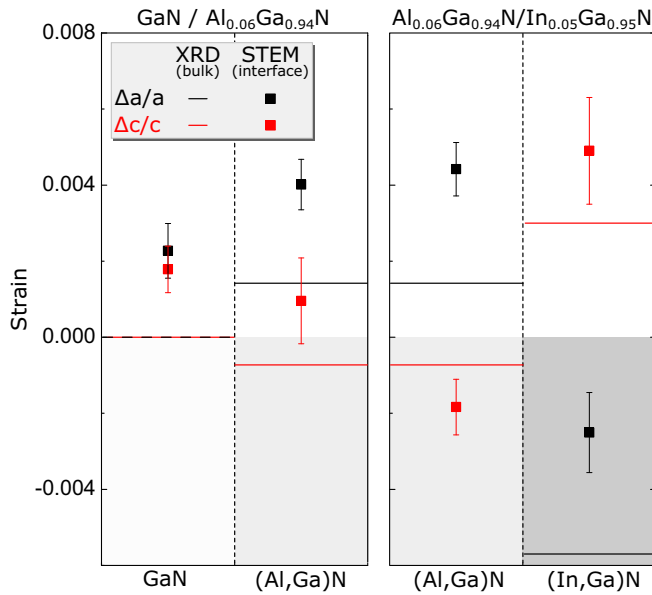


FIG. 7. Strain in the a and c directions on both sides of the $\text{Al}_{0.06}\text{Ga}_{0.94}\text{N}/\text{GaN}$ and $\text{In}_{0.05}\text{Ga}_{0.95}\text{N}/\text{Al}_{0.06}\text{Ga}_{0.94}\text{N}$ interfaces, derived from lattice constants measured by STEM in the vicinity of the interfaces, i.e., ± 5 nm (symbols) and average strain in each layer derived from XRD measurements (horizontal lines).

In contrast, the local depression points to the presence of a localized upward electrostatic potential. In the absence of any δ -doped structures, this can be induced only by negative bound charges. Bound charges can form due to interface states or due to a polarization discontinuity at the interface. Since in our sample no interface dislocations formed (biaxially strained layers; no defects detected in TEM), no interface gap states occur. Hence, only band offsets can be present, but these do not create a single depression in the phase (see the discussion about the $\text{Al}_{0.06}\text{Ga}_{0.94}\text{N}/\text{GaN}$ interface). Hence, the depression indicates a polarization change at the interface.

This is corroborated by self-consistent simulations of the phase change shown as lines in Fig. 6: Without polarization change only the steplike behavior, and not the depression, is reproduced (green line). The best agreement is found for a polarization change at the $\text{In}_{0.05}\text{Ga}_{0.95}\text{N}/\text{Al}_{0.06}\text{Ga}_{0.94}\text{N}$ interface of $+9.7 \pm 2$ mC/m² (red line in Fig. 6). Note that the surface pinning level is the same as before.

D. Strain

In order to assess the measured electron affinity and polarization changes as well as the above-mentioned MIP differences, knowledge of the strain situation at the interfaces is critical. Therefore, we first derived the strain from x-ray diffraction (XRD) measurements by analyzing the 004 reflection. Assuming a pseudomorphic growth (supported by the low Al and In compositions), we obtained *average “bulk” strain* values for the whole $\text{Al}_{0.06}\text{Ga}_{0.94}\text{N}$ and $\text{In}_{0.05}\text{Ga}_{0.95}\text{N}$ layers of $\Delta a/a = +0.0014$ and $\Delta c/c = -0.0007$ as well as $\Delta a/a = -0.0057$ and $\Delta c/c = +0.0030$, respectively. The GaN buffer layer is, as a whole, unstrained. These *average* strain values of the whole layer are visualized as solid black and red lines in Fig. 7 for the a and c directions, respectively.

Second, we derived, in addition, the *local interface strain* in the direct vicinity of the interfaces from the a and c lattice constants measured by HAADF-STEM ± 5 nm from the interface. The almost unchanged in-plane a lattice constants point to an overall biaxial strain deformation of all ternary layers, supporting the assumption of pseudomorphic growth above. This results in strain along the a and c directions, whose values in the vicinity of the interfaces are given as symbols in Fig. 7. We derived these strains on both sides of each interface using the measured lattice constants (calibrated to GaN in the substrate) and Vegard’s law for defining the unstrained lattice constants of the ternary compounds (Fig. 7).

From linear elasticity theory one expects, for biaxial strain, that the strain in the a direction ϵ_{xx} is given by the negative strain in the c direction ϵ_{zz} times the positive Poisson’s ratio ν . This is reasonably fulfilled for both the $\text{In}_{0.05}\text{Ga}_{0.95}\text{N}/\text{Al}_{0.06}\text{Ga}_{0.94}\text{N}$ interface and the adjacent average layers (although the ν values are somewhat too large). Note that the deviation between the average layer strain and the interface strain values is indicative of the local relaxation confined to the interface region.

In contrast, the $\text{Al}_{0.06}\text{Ga}_{0.94}\text{N}/\text{GaN}$ interface does not exhibit the expected biaxial strain trends as outlined above. It rather exhibits an additional hydrostatic strain component and larger deviations from the average strain of the adjacent layers (see horizontal red and black lines). This indicates an anomalous lattice relaxation being present at the $\text{Al}_{0.06}\text{Ga}_{0.94}\text{N}/\text{GaN}$ interface. Note that this lattice relaxation is present only at the interface, not in the farther away GaN buffer region.

IV. DISCUSSION

At this stage we compare the measured polarization and electron affinity changes with theoretical expectations and literature values. Therefore, we derive the expected electron affinity change on the basis of literature values: The electron affinity change is approximated by the negative conduction band offset since the vacuum energy changes only slightly with strain [34]. The conduction band change is derived from values of the composition-dependent band gap change, valence band offset [35–43], and strain-induced shift of the band edges [44,45]. In addition, a direct measurement of the electron affinity on (0001) planes was considered [46]. On this basis the electron affinity changes $\Delta\chi$ given in Table I are obtained for unstrained and biaxial strained cases. The biaxially strained values were calculated with the in-plane strain measured by HAADF-STEM given in Sec. III D. Similarly, the polarization changes are calculated following Ref. [47], taking into account the measured lattice constants.

First, we discuss the situation of unstrained interfaces: For both interfaces the measured values of the electron affinity deviate significantly from those expected for unstrained interfaces ($\text{Al}_{0.06}\text{Ga}_{0.94}\text{N}/\text{GaN}$: $\Delta\chi_{\text{measured}} = +43 \pm 50$ meV vs $\Delta\chi_{\text{unstrained}} = -89 \pm 20$ meV; $\text{In}_{0.05}\text{Ga}_{0.95}\text{N}/\text{Al}_{0.06}\text{Ga}_{0.94}\text{N}$: $\Delta\chi_{\text{measured}} = +170 \pm 50$ meV vs $\Delta\chi_{\text{unstrained}} = +279 \pm 45$ meV). The measured polarization changes for both interfaces even have the opposite sign compared to that expected for an unstrained interface.

Next, we turn to the situation of strained interfaces. For the $\text{In}_{0.05}\text{Ga}_{0.95}\text{N}/\text{Al}_{0.06}\text{Ga}_{0.94}\text{N}$ interface the measured lattice

TABLE I. Polarization and electron affinity changes at the $\text{Al}_{0.06}\text{Ga}_{0.94}\text{N}/\text{GaN}$ and $\text{In}_{0.05}\text{Ga}_{0.95}\text{N}/\text{Al}_{0.06}\text{Ga}_{0.94}\text{N}$ interfaces measured by off-axis electron holography and extracted from literature values as described in the text. The literature values are given for the unstrained and biaxially strained cases (the latter calculated using the measured in-plane strain). The polarization is defined as being positive in the [0001] direction.

Interface	Holography		Literature			
	ΔP (mC/m^2)	$\Delta\chi$ (meV)	$\Delta P_{\text{unstrained}}$ (mC/m^2)	$\Delta\chi_{\text{unstrained}}$ (meV)	$\Delta P_{\text{biaxial strain}}$ (mC/m^2)	$\Delta\chi_{\text{biaxial strain}}$ (meV)
$\text{Al}_{0.06}\text{Ga}_{0.94}\text{N}/\text{GaN}$	0 ± 2	$+43 \pm 50$	+2.3	-89 ± 20	-5.0 ± 4	-80 ± 28
$\text{In}_{0.05}\text{Ga}_{0.95}\text{N}/\text{Al}_{0.06}\text{Ga}_{0.94}\text{N}$	$+9.7 \pm 2$	$+170 \pm 50$	-16.6	$+279 \pm 45$	$+16.2 \pm 5$	$+204 \pm 46$

constants follow, in first approximation, the biaxial strain model as outlined in Sec. III D. Taking the measured strain into account, the electron affinity change expected on the basis of literature values is reduced to $+204 \pm 46$ meV, and the sign of the polarization change is reversed to $+16.2 \pm 5$ mC/m^2 (see Table I). These values agree within the error margins with the experimentally measured values of $+170 \pm 50$ meV and $+9.7 \pm 2$ mC/m^2 , respectively. The slightly smaller value of the measured polarization change suggests possible second-order deviations from the linear biaxial relaxation, which can be anticipated to reduce the polarization change.

For the $\text{Al}_{0.06}\text{Ga}_{0.94}\text{N}/\text{GaN}$ interface, however, the experimentally measured absence of polarization and electron affinity change does not agree with the theoretical expectations. This points to the importance of the anomalous strain observed in Fig. 7. In fact, it has been suggested that bound charges can induce lattice relaxation and vice versa [48]. The formation of an anomalous relaxation at the interface can be understood if one considers the principle of minimization of total energy. The total energy comprises lattice deformation and a Coulomb interaction component. The latter arises from the interaction of bound charges created by a polarization change at the interfaces. On this basis we anticipate that the $\text{Al}_{0.06}\text{Ga}_{0.94}\text{N}/\text{GaN}$ interface reduces its total energy by removing the polarization change at the interface through anomalous strain.

V. CONCLUSIONS

We have presented a methodology to characterize quantitatively polarization and electron affinity changes at group III-nitride semiconductor heterointerfaces by combining STM/STS, SIMS, off-axis electron holography in TEM, HAADF-STEM, and self-consistent calculations of the electrostatic potential and electron phase change. We demonstrated that a proper calibration of the TEM lamella's surface potentials is imperative for a quantitative measurement of potentials (bound charges, electron affinity, polarization changes, etc.) by off-axis electron holography.

This calibration can be realized by incorporating exactly known doping structures in the same sample (concentration profile and charge of impurities, band bending, etc., accessible by STM/STS and SIMS). The electron phase change profile of such known doping structures can be computed self-consistently with the only free parameter being the lamella's surface potential (pinning level). This procedure allowed us to determine the pinning level at the surfaces (i.e., amorphous-crystalline transition region) of TEM lamellae and hence quantify the so-called dead layer, which had inhibited thus far a quantitative analysis of the phase change of transmitted electrons in TEM. We found a pinning level (0.69 ± 0.2) eV above the valence band edge, which can be traced back to nitrogen vacancies created by focused ion beam preparation of the TEM lamella. With this pinning level as calibration of the lamella's surface potential, electron phase change profiles across heterointerfaces between diluted ternary group III nitride semiconductors can be quantitatively analyzed. This calibration methodology also solves the problem that, thus far, the experimental phase changes measured in electron holography have always been larger than expected since the enhancing effect of surface pinning was not quantitatively taken into account.

With this methodology we deduced quantitatively polarization and electron affinity changes at $\text{Al}_{0.06}\text{Ga}_{0.94}\text{N}/\text{GaN}$ and $\text{In}_{0.05}\text{Ga}_{0.95}\text{N}/\text{Al}_{0.06}\text{Ga}_{0.94}\text{N}$ interfaces. The $\text{In}_{0.05}\text{Ga}_{0.95}\text{N}/\text{Al}_{0.06}\text{Ga}_{0.94}\text{N}$ interface yields electron affinity and polarization changes which agree with those expected for biaxially strained layers. At the $\text{Al}_{0.06}\text{Ga}_{0.94}\text{N}/\text{GaN}$ interface no polarization change occurs, and an anomalous lattice relaxation is found. We anticipate that the underlying physical origin is the minimization of the total energy leading to a reduction of the polarization-induced bound charges at the $\text{Al}_{0.06}\text{Ga}_{0.94}\text{N}/\text{GaN}$ interface, in conjunction with an anomalous strain.

ACKNOWLEDGMENTS

The authors thank D. Eckert for helpful discussions and the Deutsche Forschungsgemeinschaft under Grant No. 398305088 for financial support.

[1] M. A. Khan, J. N. Kuznia, J. M. V. Hove, N. Pan, and J. Carter, *Appl. Phys. Lett.* **60**, 3027 (1992).

[2] R. Chaudhuri, S. J. Bader, Z. Chen, D. A. Muller, H. G. Xing, and D. Jena, *Science* **365**, 1454 (2019).

- [3] M. F. Schubert, J. Xu, J. K. Kim, E. F. Schubert, M. H. Kim, S. Yoon, S. M. Lee, C. Sone, T. Sakong, and Y. Park, *Appl. Phys. Lett.* **93**, 041102 (2008).
- [4] P. Waltereit, O. Brandt, A. Trampert, H. T. Grahn, J. Menniger, M. Ramsteiner, M. Reiche, and K. H. Ploog, *Nature (London)* **406**, 865 (2000).
- [5] H.-H. Yao, Y. Lu, K.-H. Li, F. Al-Qatari, C.-H. Liao, and X. Li, *Proc. SPIE* **10940**, 109400K (2019).
- [6] H. W. M. Salemink, O. Albrektsen, and P. Koenraad, *Phys. Rev. B* **45**, 6946 (1992).
- [7] R. M. Feenstra, D. A. Collins, D. Z.-Y. Ting, M. W. Wang, and T. C. McGill, *Phys. Rev. Lett.* **72**, 2749 (1994).
- [8] B.-C. Huang, P. Yu, Y. H. Chu, C.-S. Chang, R. Ramesh, R. E. Dunin-Borkowski, P. Ebert, and Y.-P. Chiu, *ACS Nano* **12**, 1089 (2018).
- [9] J. K. Weiss, W. J. de Ruijter, M. Gajdardziska-Josifovska, M. R. McCartney, and D. J. Smith, *Ultramicroscopy* **50**, 301 (1993).
- [10] M. R. McCartney, F. A. Ponce, and J. Cai, *Appl. Phys. Lett.* **76**, 3055 (2000).
- [11] L. Zhou, D. A. Cullen, D. J. Smith, M. R. McCartney, A. Mouti, M. Gonschorek, E. Feltin, J.-F. Carlin, and N. Grandjean, *Appl. Phys. Lett.* **94**, 121909 (2009).
- [12] S. Chung, S. R. Johnson, Y.-H. Zhang, D. J. Smith, and M. R. McCartney, *J. Appl. Phys.* **105**, 014910 (2009).
- [13] F. A. Marino, D. A. Cullen, D. J. Smith, M. R. McCartney, and M. Saraniti, *J. Appl. Phys.* **107**, 054516 (2010).
- [14] Q. Y. Wei, T. Li, J. Y. Huang, F. A. Ponce, E. Tschumak, A. Zado, and D. J. As, *Appl. Phys. Lett.* **100**, 142108 (2012).
- [15] R. E. Dunin-Borkowski, A. Kovács, T. Kasama, M. R. McCartney, and D. J. Smith, *Springer Handbook of Microscopy* (Springer, Cham, 2019), Chap. 16, pp. 767–818.
- [16] Ph. Ebert, L. Ivanova, S. Borisova, H. Eisele, A. Laubsch, and M. Dähne, *Appl. Phys. Lett.* **94**, 062104 (2009).
- [17] M. Schnedler, V. Portz, H. Eisele, R. E. Dunin-Borkowski, and Ph. Ebert, *Phys. Rev. B* **91**, 205309 (2015).
- [18] S. Landrock, Y. Jiang, K. H. Wu, E. G. Wang, K. Urban, and Ph. Ebert, *Appl. Phys. Lett.* **95**, 072107 (2009).
- [19] H.-C. Hsu, B.-C. Huang, S.-C. Chin, C.-R. Hsing, D.-L. Nguyen, M. Schnedler, R. Sankar, R. E. Dunin-Borkowski, C.-M. Wei, C.-W. Chen, P. Ebert, and Y.-P. Chiu, *ACS Nano* **13**, 4402 (2019).
- [20] L. Amichi, I. Mouton, E. Di Russo, V. Boureau, F. Barbier, A. Dussaigne, A. Grenier, P.-H. Jouneau, C. Bougerol, and D. Cooper, *J. Appl. Phys.* **127**, 065702 (2020).
- [21] W. D. Rau, P. Schwander, F. H. Baumann, W. Höppner, and A. Ourmazd, *Phys. Rev. Lett.* **82**, 2614 (1999).
- [22] Ernst Ruska-Centre for Microscopy and Spectroscopy with Electrons (ER-C), *J. Large-Scale Res. Facil.* **2**, A44 (2016).
- [23] Ernst Ruska-Centre for Microscopy and Spectroscopy with Electrons (ER-C), *J. Large-Scale Res. Facil.* **2**, A43 (2016).
- [24] M. Schnedler, V. Portz, P. H. Weidlich, R. E. Dunin-Borkowski, and Ph. Ebert, *Phys. Rev. B* **91**, 235305 (2015).
- [25] M. Schnedler, R. E. Dunin-Borkowski, and Ph. Ebert, *Phys. Rev. B* **93**, 195444 (2016).
- [26] M. Schowalter, A. Rosenauer, D. Lamoen, P. Kruse, and D. Gerthsen, *Appl. Phys. Lett.* **88**, 232108 (2006).
- [27] A. Tonomura, *Electron Holography*, 2nd ed., Springer Series in Optical Sciences (Springer, Berlin, 1999).
- [28] Q. Yan, A. Janotti, M. Scheffler, and C. G. Van de Walle, *Appl. Phys. Lett.* **100**, 142110 (2012).
- [29] S. Limpijumngong and C. G. Van de Walle, *Phys. Rev. B* **69**, 035207 (2004).
- [30] A. Kyrtosos, M. Matsubara, and E. Bellotti, *Phys. Rev. B* **93**, 245201 (2016).
- [31] J. L. Lyons and C. G. V. de Walle, *npj Comput. Mater.* **3**, 12 (2017).
- [32] L. Houben, M. Luysberg, and T. Brammer, *Phys. Rev. B* **70**, 165313 (2004).
- [33] K. Yamamoto, K. Nakano, A. Tanaka, Y. Honda, Y. Ando, M. Ogura, M. Matsumoto, S. Anada, Y. Ishikawa, H. Amano, and T. Hirayama, *Microscopy* **69**, 1 (2020).
- [34] S. Postorino, D. Grassano, M. D'Alessandro, A. Pianetti, O. Pulci, and M. Palummo, *Nanomater. Nanotechnol.* **10**, 1847980420902569 (2020).
- [35] A. Kyrtosos, M. Matsubara, and E. Bellotti, *Phys. Rev. B* **99**, 035201 (2019).
- [36] T. J. Ochalski, B. Gil, P. Lefebvre, N. Grandjean, M. Leroux, J. Massies, S. Nakamura, and H. Morkoc, *Appl. Phys. Lett.* **74**, 3353 (1999).
- [37] D. Brunner, H. Angerer, E. Bustarret, F. Freudenberg, R. Höppler, R. Dimitrov, O. Ambacher, and M. Stutzmann, *J. Appl. Phys.* **82**, 5090 (1997).
- [38] R. R. Pelá, C. Caetano, M. Marques, L. G. Ferreira, J. Furthmüller, and L. K. Teles, *Appl. Phys. Lett.* **98**, 151907 (2011).
- [39] D. Mourad and G. Czycholl, *Eur. Phys. J. B* **85**, 153 (2012).
- [40] B. Meyer, G. Steude, A. Göldner, A. Hoffmann, H. Amano, and I. Akasaki, *Phys. Status Solidi B* **216**, 187 (1999).
- [41] C. Coughlan, S. Schulz, M. A. Caro, and E. P. O'Reilly, *Phys. Status Solidi B* **252**, 879 (2015).
- [42] P. G. Moses and C. G. Van de Walle, *Appl. Phys. Lett.* **96**, 021908 (2010).
- [43] P. G. Moses, M. Miao, Q. Yan, and C. G. Van de Walle, *J. Chem. Phys.* **134**, 084703 (2011).
- [44] Q. Yan, P. Rinke, A. Janotti, M. Scheffler, and C. G. Van de Walle, *Phys. Rev. B* **90**, 125118 (2014).
- [45] Y. Cui, S. Lee, C. Freysoldt, and J. Neugebauer, *Phys. Rev. B* **92**, 085204 (2015).
- [46] S. P. Grabowski, M. Schneider, H. Nienhaus, W. Mönch, R. Dimitrov, O. Ambacher, and M. Stutzmann, *Appl. Phys. Lett.* **78**, 2503 (2001).
- [47] C. E. Dreyer, A. Janotti, C. G. Van de Walle, and D. Vanderbilt, *Phys. Rev. X* **6**, 021038 (2016).
- [48] R. E. Dunin-Borkowski, W. O. Saxton, and W. M. Stobbs, *Acta Crystallogr., Sect. A* **52**, 705 (1996).